LAWRENCE
LIVERMORE
NATIONAL
LABORATORY

LLNL-JRNL-690959

Laser-Induced Damage of Intrinsic and Extrinsic Defects by Picosecond Pulses on Multi-Layer Dielectric Coatings for Petawatt-Class Lasers

R. A. Negres, C. W. Carr, T. A. Laurence, K. Stanion, G. Guss, D. A. Cross, P. J. Wegner, C. J. Stolz

May 4, 2016

Optical Engineering

Disclaimer

Laser-Induced Damage of Intrinsic and Extrinsic Defects by Picosecond Pulses on Multi-Layer Dielectric Coatings for Petawatt-Class Lasers

Raluca A. Negres[1,*], Christopher W. Carr[1], Ted A. Laurence[1], Ken Stanion[1], Gabe Guss[1], David A. Cross[1], Paul J. Wegner[1], Christopher J. Stolz[1]

[1]Lawrence Livermore National Laboratory, 7000 East Avenue, Livermore, CA 94550, USA

Abstract. We describe a damage testing system and its use in investigating laser-induced optical damage initiated by both intrinsic and extrinsic precursors on multi-layer dielectric (MLD) coatings suitable for use in high energy, large-aperture petawatt-class lasers. We employ small-area damage test methodologies to evaluate the intrinsic damage resistance of various coatings as a function of deposition methods and coating materials under simulated use conditions. In addition, we demonstrate that damage initiation by raster scanning at lower fluences and growth threshold testing are required to probe the density of extrinsic defects which will limit large-aperture optics performance.

Keywords: Laser-induced damage, multi-layer dielectric coatings, coating defects, picosecond pulses, petawatt lasers, pulsed laser-matter interactions.

* negres2@llnl.gov

1 Introduction

There is worldwide interest in the use of high peak power/high energy laser systems[1] for a broad range of applications including direct laser writing in transparent optical materials[2,3] and driving intense secondary sources such as energetic electron beams and X-ray sources.[4–7] These applications require high laser intensities on target delivered in a short time scale and therefore pulse durations range typically from a few hundred femtoseconds (fs) up to a few tens of picoseconds (ps).[3] One of the challenges associated with the safe operation of such petawatt-class laser systems is laser-induced damage in optical components. In addition, there are outstanding issues in laser-matter interactions in the ps-pulse regime.[2,3,8] Extensive experimental and theoretical studies of laser damage with ns-pulses suggest extrinsic mechanisms (e-field enhancement due to nodular geometry) are in effect where localized absorption of incident radiation by isolated defects in the material leads to transfer of energy to the lattice and damage occurs when the deposited heat is sufficient to melt, boil or fracture the dielectric material.[8] In the fs-pulse regime, intensities corresponding to breakdown produce electrons via multi-photon and avalanche ionization and an intrinsic damage threshold of the material is sharply observed.[8] However, fewer studies have examined the relative importance of intrinsic vs. extrinsic mechanisms in the transition region of 0.5-100 ps.

The Advanced Radiographic Capability (ARC) coming online at LLNL is designed to produce energetic X-rays for backlighting experiments conducted at the National Ignition Facility (NIF).[9,10] The ARC laser system implements chirped pulse amplification and subsequent pulse compression on 4 beamlines of the NIF to produce petawatt-class short pulses (1-30 ps) at 1053 nm with a total energy of 3.2-13.6 kJ. To avoid buildup of nonlinear effects while propagating energetic short pulses in air or bulk materials, pulse compression, transport and focusing optics must rely on optical thin film mirror coatings operating in a vacuum environment. The peak irradiance of the ARC system may be limited by optical damage on these final optics, making it of great interest to

qualify their performance in their use environment and gain insight into the fundamental damage mechanisms in the ps pulse regime.

In this study, we characterize the laser-induced damage by near-IR (1053 nm), ps pulses on multi-layer dielectric (MLD), high reflectivity (HR) coatings suitable for large-aperture petawatt laser systems. We employ standard R-on-1 as well as raster scanning using a small-area beam test methodologies to quantify the intrinsic coating performance under simulated use conditions and determine whether or not damage with ps pulses is extrinsic (defect driven) in nature, as is the case with ns pulses. The results obtained from representative sub-scale witness samples can be used to inform on the multi-shot, full-scale optics performance at the ARC operation fluence.

2 Experimental Methods

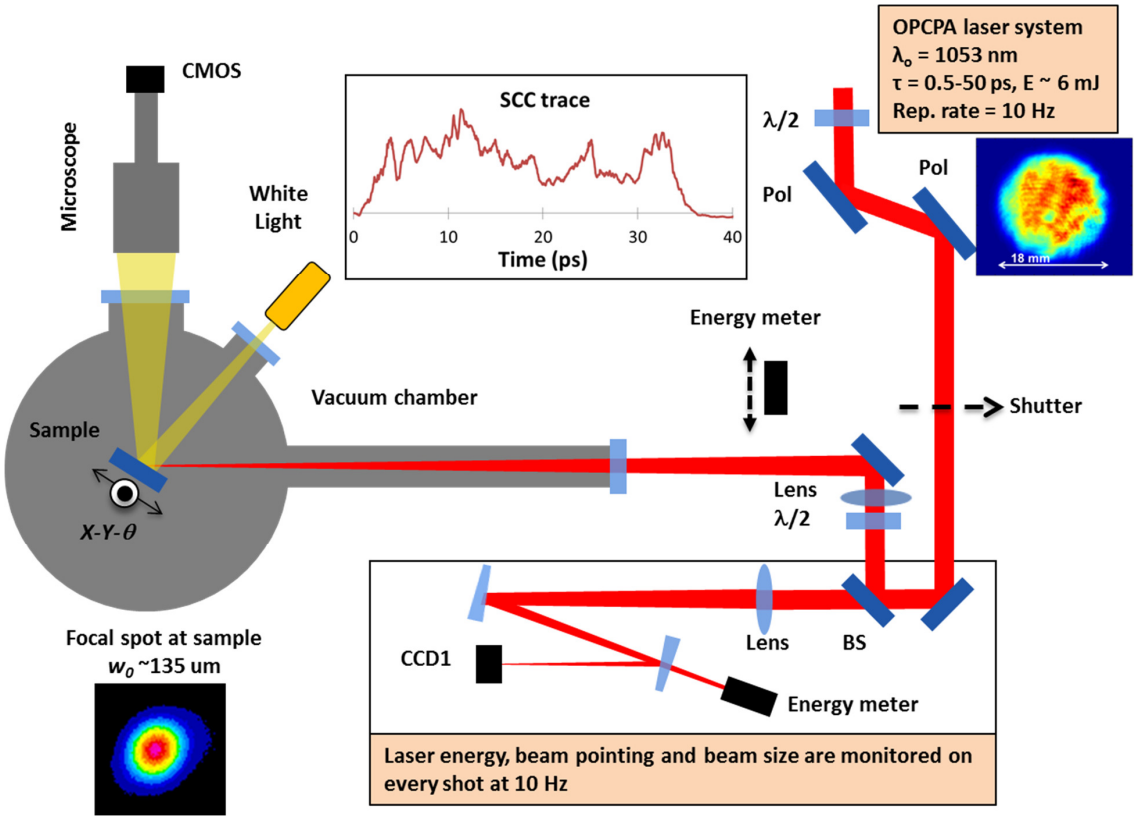

Fig 1 Schematic of vacuum damage test station driven by a 1053-nm, 10 Hz OPCPA laser system with tunable pulse duration from 0.5 ps to 50 ps. Pol - thin film polarizer, $\lambda/2$ - half-wave plate, BS - 95/5 beam-splitter, SCC scanning cross-correlator, CCD1 and CMOS sensors for beam profile monitoring and in-situ damage detection, respectively.

2.1 Damage Test Setup and Fluence Calibration

The vacuum damage test station developed at LLNL was described elsewhere[11] and is depicted schematically in Fig. 1. In brief, the output of an Optical Parametric Chirped Pulse Amplification (OPCPA) laser system[12] operating at 1053-nm, 10 Hz repetition rate with energy up to ~6 mJ per pulse and tunable duration from ~0.5 ps up to 50 ps. A 95/5 beam-splitter provides main and reference beam paths. Two thin film polarizers (Pol) eliminate residual elliptical polarization from

the beam after pulse compression and are used in combination with a motorized half-wave plate ($\lambda/2$) to provide continuous control of the energy delivered to the sample.

Most of the energy in the beam (95%) is directed towards the vacuum chamber through another half-wave plate (allows setting of S- or P-polarization per MLD coating design) and is focused at the sample plane inside the vacuum chamber via a 2-m focal length, anti-reflection (AR) coated lens. The vacuum window is a 1-cm thick, fused silica parallel plate with AR coatings. Our $f/200$ optical system results in a beam waist at the sample plane of about 135 μm (radius at 1/e^2 of maximum intensity). The sample to be tested is mounted on vacuum compatible *X-Y* motorized translation stages and a manual rotation stage (θ) at the vacuum chamber (60-cm diameter) center. In-situ damage detection is achieved via a long working distance microscope equipped with a CMOS camera and a white light illumination fiber lamp through two independent ports of the vacuum chamber. The in-situ microscope has a field of view of 1 mm^2 and spatial resolution on the order of 10 μm. The pressure in the chamber can be varied from 1 atm. (in-air, relative humidity of $\sim$40%) down to 10^{-6} torr. Although past studies have examined the effects of pressure and vacuum cleanliness on the damage performance of MLD gratings,[11] all tests discussed here were performed in a clean vacuum environment with pressures on the order of 10^{-4}-10^{-6} torr. All coatings investigated in this work were deposited on 2-inch diameter, 0.5-1 cm thick substrates and have been stored in dry N_2 atmosphere prior to their testing in vacuum for at least 48 hours.

The beam transmitted through the BS (5%) is used for diagnostics in a reference beam path to monitor both the beam energy and beam profile at an equivalent sample plane (in this case, at the center of the vacuum chamber). An identical 2-m lens focuses the low energy reference beam which is routed and attenuated using a couple of uncoated fused silica wedges (3 degrees) to a charge-couple device (CCD1 in Fig.1). As is the case for most far-field beam profile measurements using CCDs (here Basler model A102f, silicon sensor), additional neutral density filters are necessary to prevent damage to the camera sensor and maintain linearity of response in the ps-pulse regime. A reference energy meter (Coherent Inc., J-10MB-LE) is placed behind one of the wedges and is calibrated against the main energy meter (Coherent Inc., J-25MB-LE) temporarily inserted in the main beam path (see Fig. 1).

The equivalent sample plane (i.e., position of CCD1) was determined in the commissioning phase of our damage test station by comparison to a second, identical CCD placed at the vacuum chamber center in-air. The latter allowed us to determine the optimal lens position in the main beam path such as the focal plane of the lens coincides with the center of the vacuum chamber where the test sample will be mounted. Following this alignment step, we then positioned the second (reference lens) at the same distance from the BS and set the position of CCD1 at its focal plane. By performing z-scan (translation along the beam propagation direction) measurements we confirmed the position of the focal spot monitor (CCD1) is accurate within 1-2 mm of the actual sample plane. It should be noted that the Rayleigh range of the 2-m lens is about 2 cm.

Due to the inherent shot-to-shot fluctuations of the OPCPA laser, the laser energy, beam pointing and beam size need to be captured on every shot at 10 Hz. We developed a sophisticated data acquisition and controls system using LabVIEW to handle the beam diagnostics along with other tasks that need to be performed during damage tests, i.e. the number of shots delivered to the sample (via mechanical shutter), energy control via wave plate, sample navigation and in-situ damage detection with image acquisition.

The fluence at the sample plane on every shot is determined in two steps as follows. Prior to any damage test, we calibrate the reference energy meter by capturing the readings from both reference

and main energy detectors along with reference beam profiles (CCD1) for a series of shots with different energy levels. We thus determine an Energy Calibration Factor, ECF, given by the ratio of energy readings. Second, we calibrate the beam profiles acquired by CCD1 based on the shot energy (equivalent to the total counts in the image of CCD1) and count histogram to derive the peak fluence. For all tests, we report the normal beam fluence (to the propagation direction) and quote the peak fluence at the 90% level (fraction of beam energy above 90% of peak count normalized to the corresponding area using a square pixel of 6.45 μm). Our fluence measurement uncertainties originate from energy meter and camera noise and amount to about $\sim$10% error while the accuracy of the absolute fluence calibration is within 5%. The latter was further confirmed by comparison with direct, in-situ measurements of laser ablation spots on thin metallic films[13] inside the vacuum chamber under similar test conditions to the MLD coatings of interest (e.g., air or vacuum, same pulse duration).

2.2 Damage Test Procedures

The dominant mechanisms of damage (intrinsic or extrinsic) on MLD coatings in the ps-pulse regime will determine the type of measurement needed. If damage is driven by defects (extrinsic), the fluence at which damage onset is observed will depend on the test area.[14,15] This effect can be easily understood if we consider a sparse distribution of defects on the surface of an optic; the probability of encountering a defect will depend on the test area, i.e. higher for large area beams leading to a perceived lower damage threshold compared to that obtained using a smaller area beam. The standard damage test methodologies (1/1, S/1 and R/1) using a small area beam are often used due to easy access to table top lasers and the simplicity of the tests. However, the sample area tested is on the order of 10^{-3} cm^2 and thus inadequate for assessing the damage performance of meter-sized optics. In addition, the comparison between different test facilities is often difficult due to the different laser beam parameters involved. Therefore, these small beam tests provide qualitative results and are most useful in comparing samples within the same test facility, for example evaluation of different coating runs.

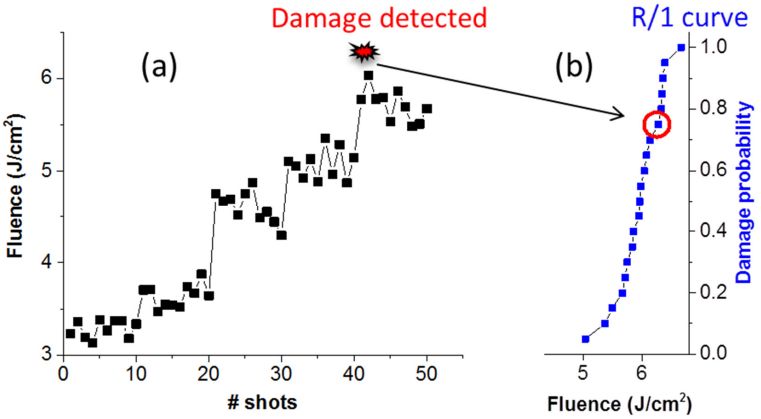

Fig 2 a) Typical 1053-nm, 30 ps laser exposure sequence during an R/1 test with 10 shots per fluence step of $\sim$0.5 J/cm^2. b) Nominal 20-site R/1 damage probability curve vs. laser fluence. Each test location is inspected in-situ (vacuum) every 10 shots; when a visible modification is detected, the test is terminated and damage is attributed to the highest peak fluence recorded at the last fluence step.

Here, we use R/1 methodology to test the onset of catastrophic damage and isolated growth

under simulated use conditions of representative MLD coatings used in large-aperture petawatt-class lasers. In Fig.2(a), we illustrate a typical fluence ramp exposure at a single site location, i.e. 10 shots per fluence step. The half-wave plate is advanced every 10 shots to increase the fraction of the beam energy directed toward the test sample. In-situ inspection of the sample surface being irradiated is performed after each sequence of 10 shots. When damage is detected (defined as a visible change at the sample' surface), the test is terminated and the highest fluence shot recorded during the last ramp step is used to construct the R/1 damage probability curve vs. fluence, as shown in Fig.2(b). The R/1 test measures the so-called laser-induced damage threshold (LIDT) and may include, by design, a laser conditioning effect due to the gradual increase in fluence at each test site; the statistics of LIDT are built by repeating the test at 20 or more different locations on the sample. It should be noted that due to shot-to-shot laser fluctuations and uncertainty in the exact shot (out of 10) that initiated laser damage, the damage site morphology varies somewhat and in most cases includes damage growth. If the starting locations chosen for R/1 tests are pristine, the results inform on the onset of catastrophic damage and provide an upper limit for the coating damage resistance. The same procedure is also useful in examining isolated locations on the sample where pre-existing flaws are observed, as is the case for μm-size defects found on MLD coatings which are introduced during the manufacturing process. For this purpose, we use the in-situ microscope to align a defect with the incident beam location and perform an R/1 test to assess whether or not those isolated defects are more prone to initiate damage and lead to damage growth upon multiple shot exposures compared to the pristine locations. We can detect the onset of damage growth and even quantify growth rate vs. fluence by using more frequent in-situ damage inspections in combination with modified fluence exposure sequences, e.g., fewer shots at each step, ramp up fluence until damage initiation occurs followed by lower fluence and/or reduced fluence step afterwards, etc.

In recent years, there has been a shift in the damage test methodologies towards quantitative damage characterization techniques via damage density measurements or so-called $\rho(\phi)$ tests which can reveal the weakest locations on the sample surface, e.g., sparsely distributed defects which damage at lower fluences than the pristine areas and are thus limiting the optics performance.[16] The $\rho(\phi)$ tests sample areas on the order of 1 cm^2 and often require a large-area beam, are more time consuming and data analysis is complex. As presented in this study, without access to a large-aperture laser facility which often implies low repetition rates, such tests can be accomplished via raster scanning using a small-area beam from a table top laser. Specifically, we simulate fluence coverage over a large area (1 cm^2 or more) by translating the sample at constant speed while the laser is free running at 10 Hz. The resulting fluence contrast at the target depends on the scan speed, the beam size and repetition rate. For our specific system, we achieve coverage at the 80% or higher peak fluence with translating the sample 100 μm between shots at 10 Hz.

Several steps are involved in the raster scanning procedure and are illustrated in Fig.3 as follows:

1. optical imaging ($\sim$1 μm spatial resolution) using a robotic microscope of the area to be scanned to identify any pre-existing flaws.
2. raster scanning at the optimal fluence level determined in prior R/1 tests (typically $\sim$80% of the minimum fluence where damage was observed).
3. re-imaging of same area (step 1) to identify any changes after raster. In Fig.3, the image is contrast enhanced to bring out some of the laser-induced modifications observed in the raster area (will be discussed in the Section 3).

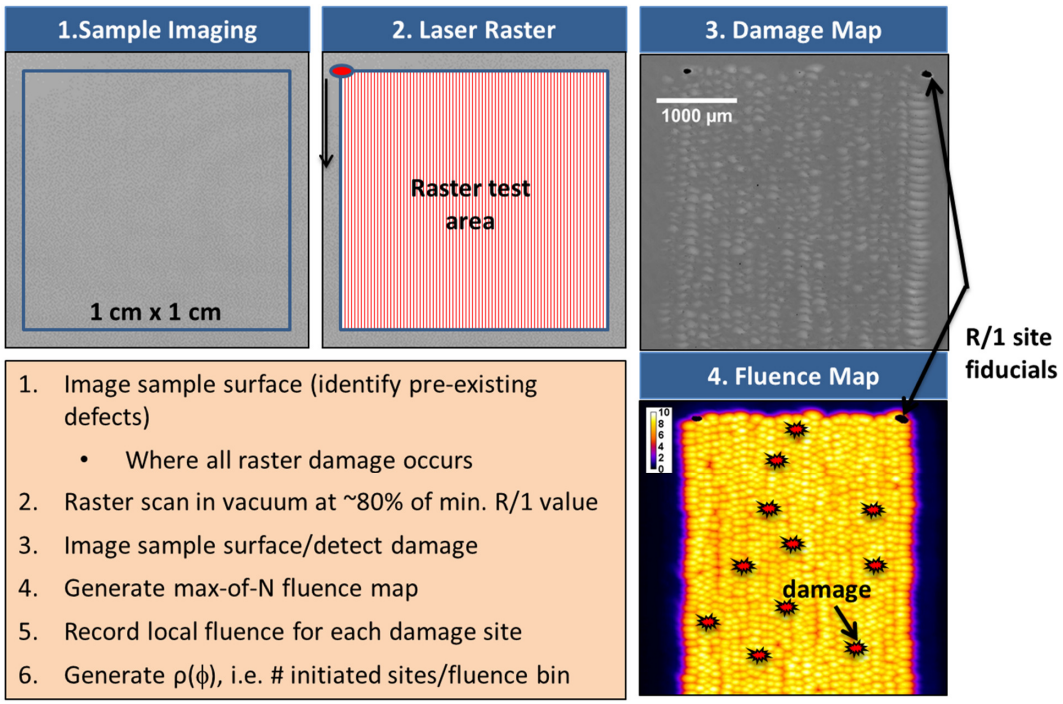

Fig 3 Step-wise procedure for raster scanning using a small beam to approximate large area testing (more details in the text).

4. generate a max-of-N fluence map using the individual calibrated fluence beam profiles acquired during the test, about ∼10,000 images for 1 cm^2 area tested. At any given location, we keep the highest fluence by convention. It should be noted, however, that a single location on the sample is exposed to several laser shots during the scan and the fluence history sequence is known. We use R/1 test locations as fiducials (reference marks) strategically placed in the corners to help in the registration of the sample and fluence maps.
5. locate any damage initiation sites (step 3) in the fluence map (step 4) and record the local fluence at each location to construct a $\rho(\phi)$ curve. We compute the number of initiated sites per fluence bin and the subsequent cumulative damage density up to any given fluence, i.e. assumes that if damage initiated at ϕ_1, it would have also initiated at ϕ_2 if $\phi_2 > \phi_1$.

3 Results and Discussion

As mentioned above, pulse compression, transport and focusing optics for high energy, petawatt-class lasers rely on optical thin film coatings operating in a vacuum environment. In addition to high damage resistance, the ability to scale the coating process to large substrates (for large aperture lasers such as ARC), stringent wavefront and spectral requirements also play a role in the selection of optical coatings for these applications.

Past experience from large-aperture laser systems (OMEGA EP, NIF, LMJ, etc.) showed MLD coatings consisting of hafnium dioxide and silicon dioxide (HfO_2/SiO_2) exhibit the best damage performance with good spectral and uniformity control.[17–20] The e-beam deposition process is typically encouraged due to the flexibility in source materials and coating designs, and relatively low cost in addition to scalability. However, thin-film stresses resulting from the optical coating process, both compressive and tensile, pose a risk to the performance and longevity of the coated

components. Specifically, e-beam coatings tend to exhibit high tensile stresses (particularly on low thermal expansion substrates in dry environments) which could lead to significant substrate deformation and potentially cracking of the coated surface (crazing in vacuum environment).[21]

We set out to investigate the damage resistance of high reflector MLD coatings manufactured by alternative deposition methods (e-beam vs. Plasma Ion Assisted Deposition or PIAD) and coating materials (hybrid, Al_2O_3 in addition to HfO_2/SiO_2) aiming to reduce the overall coating stress (i.e., densified coatings) while maintaining high damage resistance.[22–25] For this purpose, we performed R/1 tests on several mirror architectures (standard quarter-wave design for various angles of incidence, AOI, and use polarization) using 1053-nm, 30-ps pulses in vacuum at pristine coating locations. Results are shown in Fig.4 and are representative of multiple samples of each coating type (from different coating runs, not all shown). Measurement errors are nominally ∼10%. The data points at 0% damage probability for 58°, S-polarization high reflector indicate no damage up to ∼15 J/cm^2, the maximum fluence currently available in our damage test setup. These results suggest that the damage performance i) from densified coatings is lower compared to HfO_2/SiO_2 e-beam coatings for same use conditions, ii) varies with AOI and polarization, with 45-degree P-reflectors being most challenging. The latter trends are in part correlated with the inverse dependence on AOI of the E-field distribution in the top layers and the increased penetration depth into the layer stack of P- vs. S-polarized light and deserve further investigation using other coating designs and AOI. It should be noted that the damage resistance of pristine areas on all types of coatings illustrated in Fig.4 is satisfactory when compared to the typical average operational fluence of most petawatt-class lasers of ∼2-3 J/cm^2. However, as discussed next, other limiting factors need to be considered when evaluating the damage performance of large-area optics.

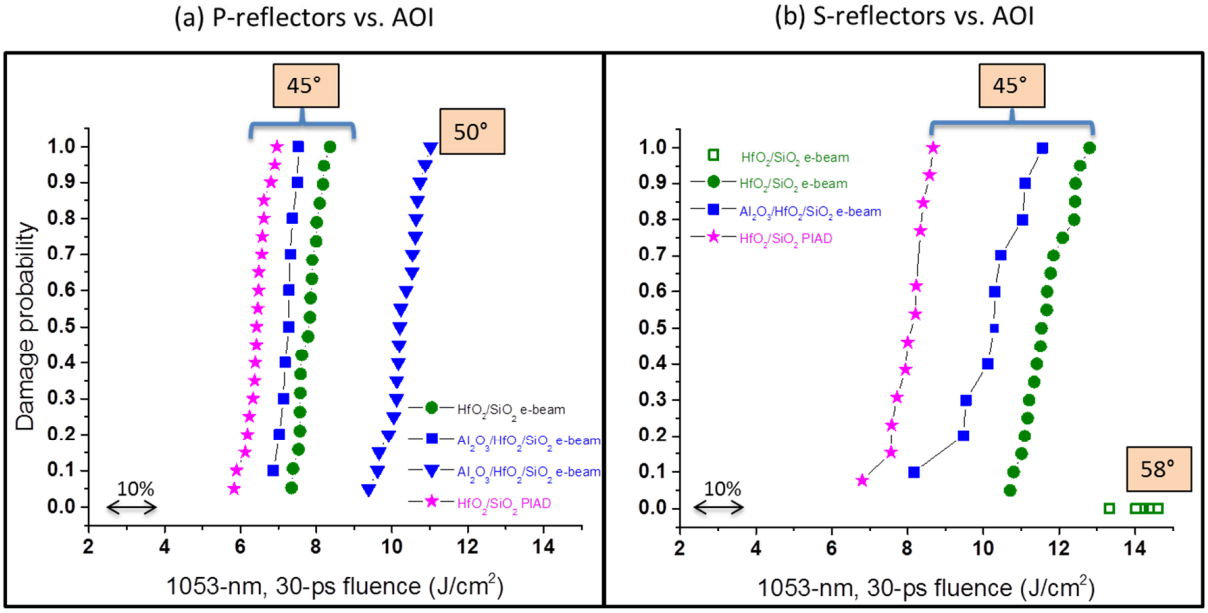

Fig 4 The damage performance of various MLD coatings as a function of deposition methods (e-beam or PIAD), materials (alternating layers of HfO_2/SiO_2, or Al_2O_3 layers distributed throughout the HfO_2/SiO_2 stack by replacing some of the HfO_2 layers), and architecture: a) P-reflectors and b) S-reflectors, respectively. All R/1 tests were performed in vacuum using 1053-nm, 30-ps pulses at the use polarization and AOI.

Although we have examined the damage performance over extended areas in all coating sam-

ples above using raster scanning, here we limit our discussion to one case study. Specifically, we present the test results and detailed characterization of laser-induced modifications (damage) from an $Al_2O_3/HfO_2/SiO_2$ e-beam HR coating designed for AOI = 50°, P-pol (see Fig. 5, all results obtained in vacuum with 1053-nm, 30-ps pulses).

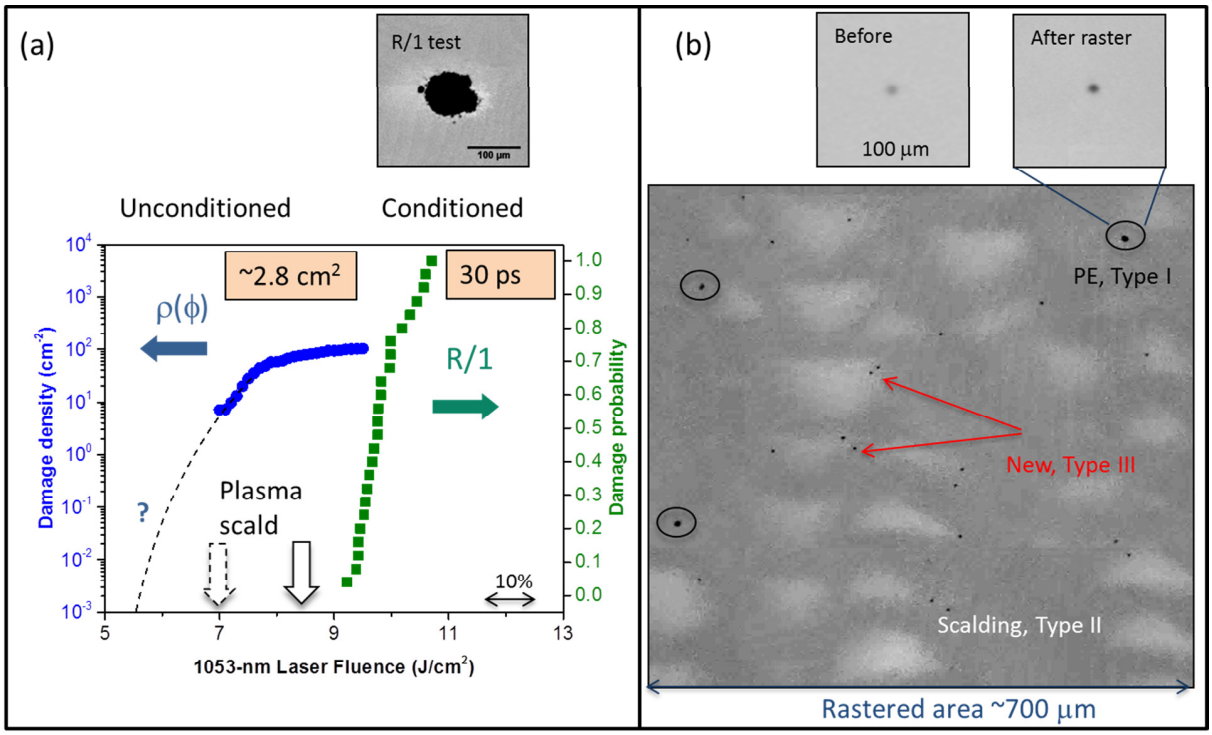

Fig 5 a) In vacuum, 1053-nm, 30-ps R/1 damage probability and $\rho(\phi)$ damage density (defect driven, see text) measurements vs. fluence in $Al_2O_3/HfO_2/SiO_2$ e-beam HR coating designed for AOI = 50°, P-pol. b) Ex-situ optical microscope image of a 700 x 700 μm^2 region of the rastered area (contrast enhanced) illustrating three types of laser-induced modifications observed in this coating sample: darkening of PE defects (black circles, Type I), onset of plasma scalding over extended areas (white regions, Type II) and new pinpoint damage initiations (indicated by red arrows, Type III).

First, an R/1 test was performed at pristine coating locations. The onset of catastrophic damage to the coating was observed at about 9 J/cm^2 while the 50% damage probability fluence was ~10.2 J/cm^2 as shown in Fig. 5(a). By design, the R/1 test provides an upper limit on the coating damage performance as the fluence is gradually increased at any given location and leads to laser conditioning of the irradiated area.

We then used the minimum fluence of the R/1 curve to guide the optimal fluence for raster scanning at the next step, in this case between 7-8.5 J/cm^2 over multiple areas totaling up to ~2.8 cm^2. Note that irradiation at the raster scan fluences occurs primarily on pristine areas without prior exposure to lower fluences, therefore these tests probe the damage performance of largely unconditioned coating material, in contrast to the R/1 tests above. Several types of laser-induced modifications (damage) were observed in the rastered area and are competing at these test fluences (see Fig. 5(b)): I) darkening of μm-size, pre-existing (PE) coating defects (compared to their appearance before raster); II) onset of plasma scalding over extended areas; III) new pinpoint damage initiations in the areas of Type II damage. Only Type I damage initiation was counted towards the

damage density curve plotted in Fig. 5(a), however, we do not know if these sites will continue to evolve upon subsequent laser exposure. We hypothesize that Type I damage features represent ejection of nodular defects and may be stable up to a threshold irradiation fluence but grow in size at higher exposures (see additional tests below). This defect-driven $\rho(\phi)$ curve saturates at higher fluences as all the isolated defects encountered in the tested area initiate ($\sim$200 per cm^2 on this sample) while its behavior at lower fluences is unknown. The dotted line in Fig. 5(a) represents an extrapolation to much lower damage densities of $\sim 10^{-3}$ cm^{-2} (relevant to large area optics) based on the observation that no damage occurred over $\sim$0.4 cm^2 tested at 5.5-6 J/cm^2. The onset of plasma scalding (Type II damage) in the raster areas over extended areas was observed at about 7 J/cm^2. In contrast, scalding occurred at fluences above 8.5 J/cm^2 during R/1 tests due to laser conditioning effects associated with the latter test (see wide arrows in Fig. 5(a), dotted and solid lines for unconditioned vs. conditioned coating material, respectively). Moreover, many new damage pinpoints ($\sim$1 μm in size) were observed in the plasma scalded regions (Type III) but were not counted towards the damage density curve. While Type I damage at isolated coating defects may be acceptable for large-aperture lasers, Type II and III damage represent the onset of catastrophic failure of the coating over extended areas and should be avoided. The effectiveness of laser conditioning on all these types of damage warrants further examination in future work.

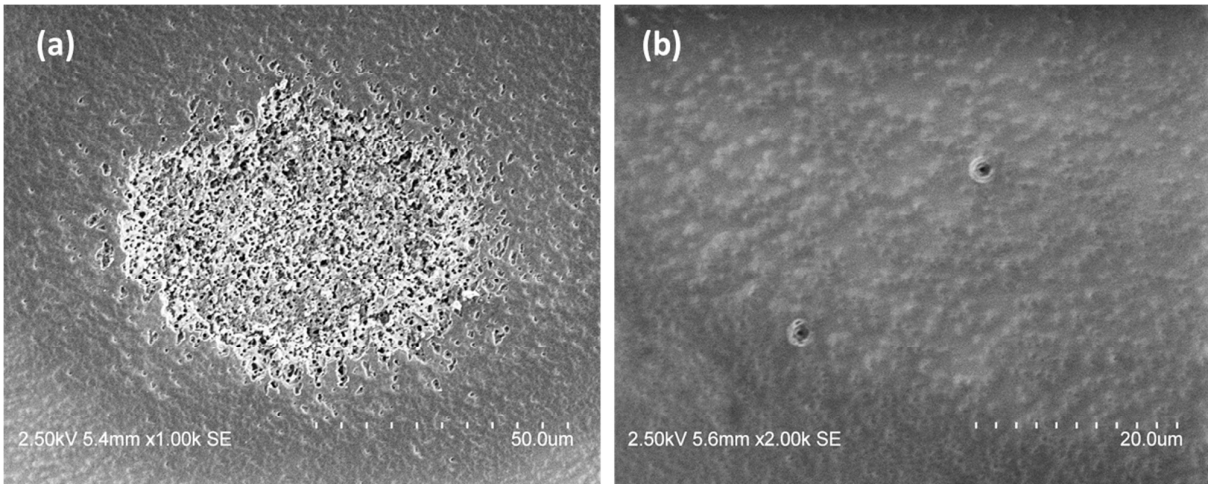

Fig 6 SEM imaging of (a) a typical R/1 site and (b) small area within a 1-cm^2 raster which contains Type III damage on the same coating sample as in Fig. 5. Charging of the dielectric surface causes artificial contrast in these images.

The laser-induced modifications in the raster area are very subtle and not resolved by optical microscopy. SEM images of various test regions on the same coating sample are shown in Fig. 6. The catastrophic damage observed at R/1 sites is clearly a prominent central feature in Fig. 6(a) surrounded by scalding of the coating top-layer which extends radially out to $\sim$150 μm, in agreement with the near-Gaussian beam profile. In contrast, the higher resolution image of a small area within the raster reveals two discrete, Type III damage initiations in a field of plasma scalding (see Fig. 6(b)). Such small discrete features can be explained in the context of pulse scaling of damage initiation and growth as well as the limited number of laser exposures at any given location on the sample during the raster (compared to the R/1 test), i.e., long, ns pulses initiate larger damage sites which can grow in larger quanta per shot compared to short, ps pulses.[26–28]

To address the question of whether or not these isolated initiation sites grow upon subsequent

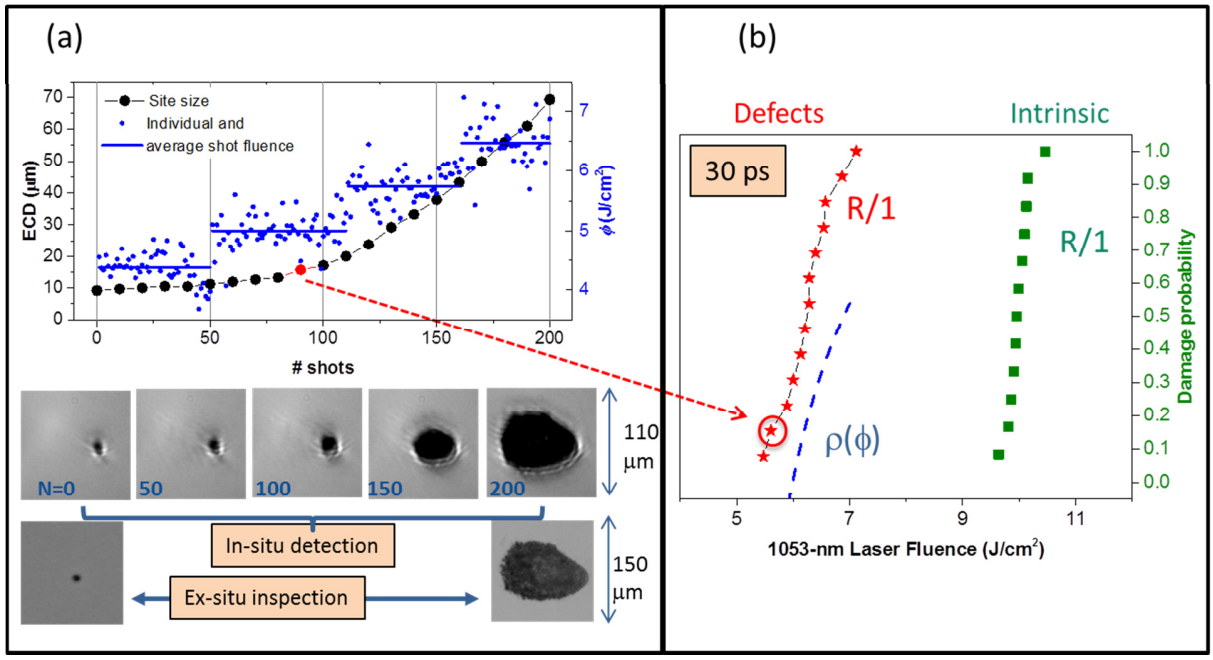

Fig 7 a) A typical damage growth sequence using 30-ps, 1053-nm pulses in vacuum at a pre-existing coating defect location on the $Al_2O_3/HfO_2/SiO_2$ coating. In-situ microscope images reveal the onset of sustained growth after ~90 shots and provide estimates of growth rate. b) Damage probability curves via R/1 tests measured from this coating sample at pristine (green squares) and defect (red stars) locations, respectively. The low fluence tail of the damage density curve $\rho(\phi)$ is also shown for comparison (dotted blue line).

exposure, we employed R/1 methodology to target individual coating defects (on a different sample with the same coating design as that shown in Fig. 5) to test the onset fluence for damage growth under simulated use conditions (may include laser conditioning). We rely on the in-situ microscope (detection limit of ~10 μm) to detect and quantify changes at defect locations upon laser exposure in vacuum; as such, each test location was exposed to 50 laser shots at each fluence step with inspections every 10 shots. Most growth tests were limited to about 200 shots to maintain a small site diameter compared to the beam area (ideally, damage growth experiments are conducted under flooded fluence conditions using a large area beam[28]). The growth rate measurements using a small, Gaussian beam are most meaningful within the central area associated with its peak fluence. As the site continues to grow from several microns to tens of microns in diameter, its area is exposed to a strong gradient of fluence and growth at the site periphery slows down compared to its center. More involved test procedures can be designed to overcome this limitations, such as successive raster scans over 1-2 mm^2 area containing the defect with increasing fluence.

The results are presented in Figs. 7(a)-(b). A typical growth sequence with site diameter (ECD, in μm, black circles) and laser exposure fluence at 1053-nm, 30 ps pulses (blue dots, lines indicate average fluence at each step) vs. number of shots is shown in Fig. 7(a). In addition, several in-situ images of the tested area captured every 50 shots are included to illustrate the evolution of the defect site size with laser exposures. The pre- and post-test ex-situ inspection images reveal the damage site morphology with 1 μm resolution for comparison to in-situ inspections. No significant changes in the site size were observed at exposure fluences below ~5 J/cm^2. Upon increasing the fluence exposure, the damage site increases in size at a slow rate and growth appears to be sustained

beyond shot 90. The onset of damage growth is thus assigned to the highest peak fluence during the previous 10 shots (80-90) and is used to construct the R/1 damage probability curve due to PE defects (dotted arrow). The test was repeated at multiple defect locations to build statistics and the results are shown in Fig. 7(b) as follows: R/1 curve for defects to be compared with the R/1 curve obtained at pristine coating locations (red stars and green squares, respectively) and the low-fluence tail of the damage density curve (dotted blue line), all measured on the same coating sample. The general observations regarding damage growth at isolated defect locations on the $Al_2O_3/HfO_2/SiO_2$ coating at 50°, P-pol, 30-ps pulses in vacuum can be summarized as follows:

i) PE defects change slightly but remain stable up to 50-100 shots at fluences at or below 5 J/cm^2; similar changes were observed during raster scanning (with 1-2 higher fluence shots), see Fig 5(b) for Type I damage (most probably similar to a gentle nodular ejection, as observed for the case of sub-growth threshold, ns-pulse damage of artificial nodular defects[29,30]).

ii) at higher fluences (>5 J/cm^2), damage growth at defect locations proceeds at a slow rate. We estimate that the damage site diameter increases by ∼20-30 μm every 50 shots at fluences between ∼5.5 and 7.5 J/cm^2.

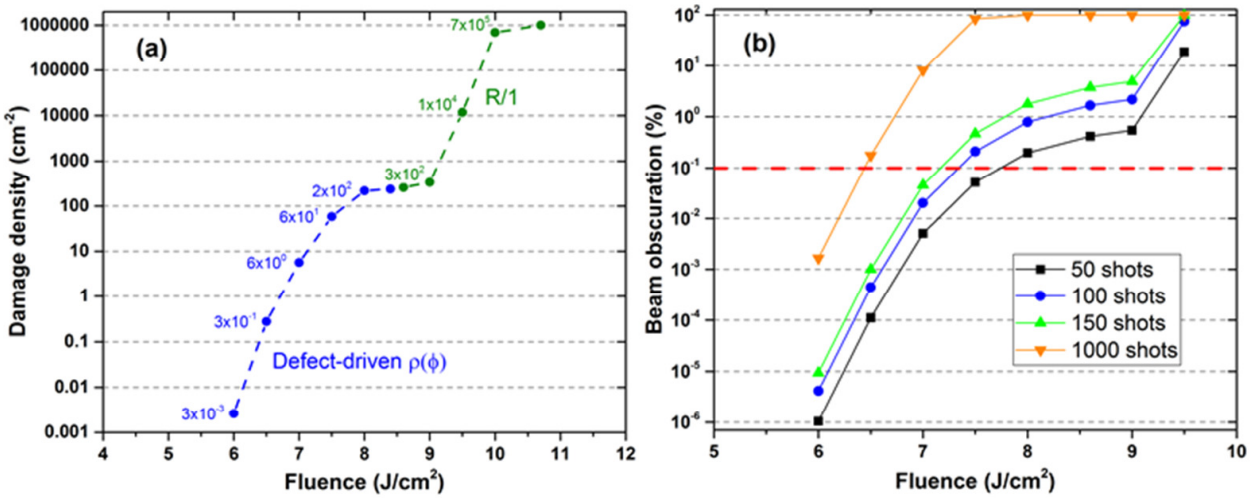

Fig 8 a) Approximated damage density vs. fluence (see text for details) over a larger range of laser fluences for the $Al_2O_3/HfO_2/SiO_2$ coating to include damage from multiple sources : isolated coating defects (defect-driven $\rho(\phi)$, dotted blue line) and pristine coating failure (catastrophic damage via R/1 testing, dotted green line). The damage density predictions for selected fluences (solid data points) are also shown. b) Percent of beam area obscuration vs. number of shots at constant fluences using the damage density prescribed in a) and the estimated growth rates with 30-ps pulses.

Next, we will use the $Al_2O_3/HfO_2/SiO_2$ coating as a case example to estimate the impact of various sources of damage on the performance of large-area coated optics under multiple laser exposures. For this exercise, we extend the damage density vs. fluence curve over a larger range of laser fluences based on the observed damage behaviors in Figs. 5-7. Namely, the defect-driven $\rho(\phi)$ can be approximated by a power law (coefficient ∼9) with onset at ∼6 J/cm^2 followed by saturation beyond ∼8 J/cm^2 as all PE defects present on the optic have initiated damage (dotted

blue line in Fig. 8(a)). Next, we make use of the R/1 damage probability and its fluence span to simulate equivalent damage densities at these higher test fluences as follows: the curve is stretched vertically such that the 0% probability coincides to the saturation density level of the $\rho(\phi)$ while the 100% probability corresponds to an arbitrary high damage density, i.e. $\sim$250 and 10^6 sites/cm^2, respectively (dotted green line in Fig. 8(a)). It can be seen that the latter addition to the damage density curve is extremely steep as it represents the onset of catastrophic failure in the pristine coating. This last step is of particular value if the laser system for which damage performance is being estimated has significant contrast on its beam. We now have a mathematical construct to approximate the damage initiation density for arbitrary fluences. Several prediction values (solid data points) are noted in Fig. 8(a). In addition, we have observed a slow, fairly constant rate of increase in the site diameter under multiple, 30-ps laser exposures (see Fig. 7(a)). Let us also assume a simplified fluence dependence to the growth rate per 50 shots as follows: 20 μm, 30 μm and 40 μm for three different fluence ranges, 5.5-6.5 J/cm^2, 7-8 J/cm^2 and 8.5-9.5 J/cm^2, respectively.

We can now estimate the percentage of beam area obscuration (due to sizable damage sites) vs. number of shots at constant fluence as: $\rho(\phi)[\text{cm}^{-2}] \times ECD[\text{cm}^2] \times 100$. This quantity is plotted in Fig. 8(b) where 100% value on the y-axis corresponds to the entire optic being damaged. A beam obscuration up to about 0.1% (dotted red line in Fig. 8(b)) is typically acceptable for large aperture, low repetition rate petawatt-class lasers. This relaxed constraint combined with anticipated average operational fluences below 4 J/cm^2 suggests that damage initiation and growth due to isolated coating defects will not curtail the lifetime of optical components for years of laser operation. However, other types of damage precursors, such as particulate contaminants in the beamline[31] and plasma scalding over large areas, along with high beam contrast (static and dynamic) and shorter pulse duration could accelerate the degradation of the optics. These issues and required mitigation methods will be addressed in future studies.

4 Summary

We described a vacuum damage test capability to examine MLD coatings performance under conditions similar to those present on ps, petawatt-class lasers. Small beam (R/1) testing was employed to test intrinsic damage thresholds of optical coatings of various architectures and use conditions. Raster scanning over 1+ cm^2 revealed damage onset at isolated defects for all MLD coatings tested here, i.e. the use fluence is limited by damage of extrinsic precursors. The two techniques are complementary in that the small beam test allows both the laser designer to select the best MLD architecture for a particular use condition and the experimenter to determine what fluence to conduct the raster test at, while the raster technique provides information about how a given run of material will actually perform and helps establish safe operational limits for the laser.

Acknowledgments

This work was performed under the auspices of the U.S. Department of Energy (DOE) by Lawrence Livermore National Laboratory under Contract DE-AC52-07NA27344. LLNL-JRNL-690959

References

1 C. Danson, D. Hillier, N. Hopps, *et al.*, "Petawatt class lasers worldwide," *High Power Laser Science and Engineering* **3**, e3 (2015). [doi:10.1017/hpl.2014.52].

2 R. R. Gattass and E. Mazur, "Femtosecond laser micromachining in transparent materials," *Nat. Photon.* **2**, 219–225 (2008). [doi:10.1038/nphoton.2008.47].

3 X. Liu, D. Du, and G. Mourou, "Laser ablation and micromachining with ultrashort laser pulses," *IEEE J. Quantum. Elect.* **33**, 1706–1716 (1997). [doi:10.1109/3.631270].

4 J. W. Dawson, J. K. Crane, M. J. Messerly, *et al.*, "High average power lasers for future particle accelerators," *AIP Conf. Proc* **1507**, 147–153 (2012). [doi:10.1063/1.4773687].

5 S. M. Hooker, "Developments in laser-driven plasma accelerators," *Nat. Photon.* **7**, 775–782 (2013). [doi:10.1038/nphoton.2013.234].

6 C. Benedetti, C. B. Schroeder, E. Esarey, *et al.*, "Plasma wakefield driven by an incoherent combination of laser pulses: A path towards high-average power laser-plasma accelerators," *Phys. Plasmas* **21**, 056706 (2014). [doi:10.1063/1.4878620].

7 M. Borghesi, A. Bigongiari, S. Kar, *et al.*, "Laser-driven proton acceleration: source optimization and radiographic applications," *Plasma Phys. Control. Fusion* **50**, 124040 (2008). [doi:10.1088/0741-3335/50/12/124040].

8 B. C. Stuart, M. D. Feit, S. Herman, *et al.*, "Nanosecond-to-femtosecond laser-induced breakdown in dielectrics," *Phys. Rev. B* **53**, 1749–1761 (1996). [doi:10.1103/PhysRevB.53.1749].

9 J. M. D. Nicola, S. T. Yang, C. D. Boley, *et al.*, "The commissioning of the advanced radiographic capability laser system: experimental and modeling results at the main laser output," *Proc. SPIE* **9345**, 93450I (2015). [doi: 10.1117/12.2080459].

10 C. Haefner, J. E. Heebner, J. Dawson, *et al.*, "Performance measurements of the injection laser system configured for picosecond scale advanced radiographic capability," *J. Phys. Conf. Ser.* **244**, 032005 (2010). [doi:10.1088/1742-6596/244/3/032005].

11 D. A. Alessi, C. W. Carr, R. P. Hackel, *et al.*, "Picosecond laser damage performance assessment of multilayer dielectric gratings in vacuum," *Opt. Express* **23**, 15532–15544 (2015). [doi: 10.1364/OE.23.015532].

12 I. Jovanovic, C. Brown, B.Wattellier, *et al.*, "Precision short-pulse damage test station utilizing optical parametric chirped-pulse amplification," *Rev. Sci. Instrum.* **75**, 5193 (2004). [doi:10.1063/1.1819382].

13 I. L. Bass, R. A. Negres, K. Stanion, *et al.*, ""Metallic burn paper" used for *in situ* characterization of laser beam properties," *Appl. Opt.* **55**, 3131–3139 (2016). [doi:10.1364/AO.55.003131].

14 M. D. Feit, A. M. Rubenchik, M. R. Kozlowski, *et al.*, "Extrapolation of damage test data to predict performance of large-area nif optics at 355 nm," *Proc. SPIE* **3578**, 1–9 (1999). [doi: 10.1117/12.344413].

15 T. A. Laurence, J. D. Bude, S. Ly, *et al.*, "Extracting the distribution of laser damage precursors on fused silica surfaces for 351 nm, 3 ns laser pulses at high fluences (20-150 j/cm^2)," *Opt. Express* **20**, 11561–11573 (2012). [doi: 10.1364/OE.20.011561].

16 C. W. Carr, M. D. Feit, M. C. Nostrand, *et al.*, "Techniques for qualitative and quantitative measurement of aspects of laser-induced damage important for laser beam propagation," *Meas. Sci. Technol.* **17**, 1958–1962 (2006). [doi:10.1088/0957-0233/17/7/039].

17 J. B. Oliver, J. Howe, A. Rigatti, *et al.*, "High precision coating technology for large aperture NIF optics," in *Optical Interference Coatings*, ThD2, Optical Society of America (2001). [doi:10.1364/OIC.2001.ThD2].

18 J. Oliver, A. Rigatti, J. Howe, *et al.*, "Thin-film polarizers for the omega ep laser system," *Proc. SPIE* **5991**, 599119 (2006). [doi:10.1117/12.638809].

19 J. B. Oliver, S. Papernov, A. W. Schmid, *et al.*, "Optimization of laser-damage resistance of evaporated hafnia films at 351 nm," *Proc. SPIE* **7132**, 71320J (2008). [doi:10.1117/12.805383].

20 B. Pinot, H. Leplan, F. Houbre, *et al.*, "Laser megajoule 1.06-μm mirrors production with very high laser damage threshold," *Proc. SPIE* **4679**, 234–241 (2002). [doi:10.1117/12.461687].

21 H. Leplan, B. Geenen, J. Y. Robic, *et al.*, "Residual stresses in evaporated silicon dioxide thin films: Correlation with deposition parameters and aging behavior," *J. Appl. Phys.* **78**, 962968 (1995). [doi:10.1063/1.360290].

22 D. J. Smith, M. McCullough, C. Smith, *et al.*, "Low stress ion-assisted coatings on fused silica substrates for large aperture laser pulse compression grating," *Proc. SPIE* **7132**, 71320 (2008). [doi:10.1117/12.817336].

23 E. Lavastre, J. Néauport, J. Duchesne, *et al.*, "Polarizers coatings for the Laser MegaJoule prototype," in *Optical Interference Coatings*, TuF3, Optical Society of America (2004). [doi:10.1364/OIC.2004.TuF3].

24 J. B. Oliver, P. Kupinski, A. L. Rigatti, *et al.*, "Modification of stresses in evaporated hafnia coatings for use in vacuum," in *Optical Interference Coatings*, WD6, Optical Society of America (2010). [doi:10.1364/OIC.2010.WD6].

25 J. B. Oliver, P. Kupinski, A. L. Rigatti, *et al.*, "Stress compensation in hafnia/silica optical coatings by inclusion of alumina layers," *Opt. Express* **20**, 16596–16610 (2012). [10.1364/OE.20.016596].

26 C. W. Carr, D. A. Cross, M. A. Norton, *et al.*, "The effect of laser pulse shape and duration on the size at which damage sites initiate and the implications to subsequent repair," *Opt. Express* **19**, A859A864 (2011). [10.1364/OE.19.00A859].

27 C. W. Carr, J. B. Trenholme, and M. L. Spaeth, "Effect of temporal pulse shape on optical damage," *Appl. Phys. Lett.* **90**, 041110 (2007). [10.1063/1.2431705].

28 R. A. Negres, M. A. Norton, D. A. Cross, *et al.*, "Growth behavior of laser-induced damage on fused silica optics under uv, ns laser irradiation," *Opt. Express* **18**, 19966–19976 (2010). [doi:10.1364/OE.18.019966].

29 X. Cheng, A. Tuniyazi, J. Zhang, *et al.*, "Nanosecond laser-induced damage of nodular defects in dielectric multilayer mirrors [Invited]," *Appl. Opt.* **53**, A62–A69 (2014). [doi: 10.1364/AO.53.000A62].

30 X. Cheng, H. Ma, A. Tuniyazi, *et al.*, "A comparative study of the laser-induced damage characteristics of artificial nodules prepared by different processes," Paper 9632–6, presented at SPIE Laser Damage (2015).

31 S. R. Qiu, M. A. Norton, R. N. Raman, *et al.*, "Impact of laser-contaminant interaction on the performance of the protective capping layer of 1ω high-reflection mirror coatings," *Appl. Opt.* **54**, 8607–8616 (2015). [doi : 10.1364/AO.54.008607].

List of Figures

8 a) Approximated damage density vs. fluence (see text for details) over a larger range of laser fluences for the $Al_2O_3/HfO_2/SiO_2$ coating to include damage from multiple sources : isolated coating defects (defect-driven $\rho(\phi)$, dotted blue line) and pristine coating failure (catastrophic damage via R/1 testing, dotted green line). The damage density predictions for selected fluences (solid data points) are also shown. b) Percent of beam area obscuration vs. number of shots at constant fluences using the damage density prescribed in a) and the estimated growth rates with 30-ps pulses.

Raluca A. Negres